Ravi Mullapudi and Ayoub
Int J Concr Struct Mater (2018) 12:61
https://doi.org/10.1186/s40069-018-0286-z

International Journal of Concrete Structures and Materials

ORIGINAL ARTICLE

Open Access

Fiber Beam Analysis of Reinforced Concrete Members with Cyclic Constitutive and Material Laws

T. Ravi Mullapudi[1] and Ashraf Ayoub[2*]

Abstract

This paper presents a non-linear Timoshenko beam element with axial, bending, and shear force interaction for nonlinear analysis of reinforced concrete structures. The structural material tangent stiffness matrix, which relates the increments of load to corresponding increments of displacement, is properly formulated. Appropriate simplified cyclic uniaxial constitutive laws are developed for cracked concrete in compression and tension. The model also includes the softening effect of the concrete due to lateral tensile strain. To establish the validity of the proposed model, correlation studies with experimentally-tested concrete specimens have been conducted.

Keywords: combined loading, Timoshenko beam, R/C beams, uni-axial constitutive relations, tangent stiffness

1 Background

The response of reinforced concrete (RC) structures is affected by the combined effect of bending, shear, and axial loads. Accurate constitutive model of RC elements for combined loadings is essential for reliably predicting structural behavior. In the past decades constitutive models have markedly improved, thereby improving the accuracy and efficiency of modeling complex RC structures. Efficient constitutive models for concrete and reinforcing bars are typically established from large-scale panel testing, and assuming a smeared cracked behavior. Belarbi and Hsu (1995) developed the Rotating-Angle Softened-Truss Model (RA-STM). They assumed that shear stresses exist along the crack direction, and proposed a tension stiffening function to account for this effect. This model was further improved by Pang and Hsu (1996), who developed the Fixed-Angle Softened-Truss Model (FA-STM). In this model, cracks were assumed to be oriented at a fixed angle. Zhu et al. (2001) derived a proper shear modulus compatible with the FA-STM model and proposed a robust solution algorithm for analysis of shear-critical concrete elements. Later, the authors evaluated the Hsu/Zhu Poisson's Ratio (Poisson's ratio for cracked concrete) (Zhu and Hsu 2002), which resulted in the Softened Membrane Model (SMM). The SMM proved to be able to simulate both the pre-peak and post-peak behavior of concrete elements.

Accurate modeling of the complex behavior of RC structures is typically performed with two-dimensional membrane elements. However, these elements are computationally very expensive, which renders the analysis time-consuming. Unlike membrane elements, fiber beam elements proved to provide a good balance between accuracy and numerical efficiency (Belarbi and Hsu 1995). In fiber-based beam elements, the spread of inelasticity along the depth is evaluated through discretization of the section into a large number of fibers with appropriate material models. Typical fiber elements account for the axial-flexural interaction effect owing to the assumption that plane sections remain plane after deformation. Lately, Mullapudi and Ayoub (Mullapudi and Ayoub 2010) developed a fiber-based beam element that accounts for shear-axial-flexure interaction effects and further improved the element to account for full three-dimensional effects, including the combined bending, axial, shear and torsional interaction (Mullapudi and Ayoub 2013).

*Correspondence: Ashraf.Ayoub.1@city.ac.uk
[2] Dept. of Civil Engineering, City University of London, Northampton Square, London EC1V OHB, UK
Full list of author information is available at the end of the article
Journal information: ISSN 1976-0485 / eISSN 2234-1315

2 Research Objective

The main objective of this paper is to derive an appropriate material tangent stiffness matrix for fiber beam-column element formulation of shear-critical concrete members (Fig. 1). The developed stiffness matrix does not account for material nonlinearity. Simplified cyclic uniaxial constitutive laws are developed for concrete in both compression and tension. The formulation of the proposed element is based on the flexibility method of analysis. Flexibility-based formulations (Mullapudi and Ayoub 2009; Labib et al. 2013) are used to overcome most of the locking difficulties associated with the standard displacement model. Shear effects is simulated through a Timoshenko-based approach (Mullapudi and Ayoub 2009). The concrete constitutive law is based on the aforementioned SMM model with Hsu/Zhu ratios. The work also attempts to improve the development of the concrete uni-axial constitutive relations. The model is added to the library of the finite element program FEAPpv (Taylor 2005).

3 Concrete Constitutive Model

The ACI 318 (American Concrete Institute 2008) building code suggests that the shear strength of an RC member is the combination of concrete strength (V_C) and transverse reinforcement strength (V_S). The value of V_C cannot be calculated in the RA-STM model, because the crack angle is assumed to be rotating. However, the FA-STM and SMM theories are capable of accounting for the effect of V_C; because the cracks are assumed to be oriented at a fixed angle and the proper concrete shear stress term (τ_c) is accounted for.

To formulate the SMM model with the inclusion of FRP, three coordinate systems are defined as shown in Fig. 2: the first (x, y) represents the local coordinate of the fiber; the second (1, 2) defines the principal stresses; while the third system (r, d) defines the concrete principal coordinate system in which the concrete shear stress $\tau^c_{12} = 0$. In the figure, α_1 is the angle between the x- and 1-axes, and α_r is the angle between the x- and r-axes (Fig. 2).

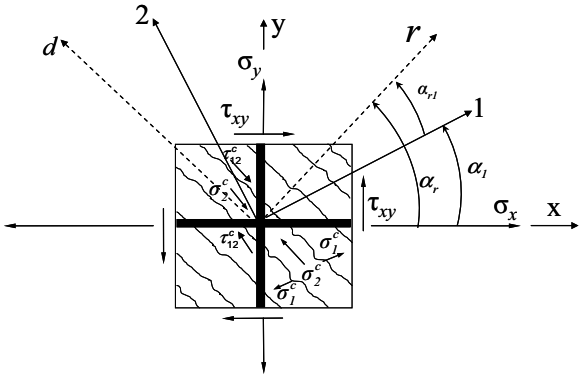

Fig. 2 Local coordinate (x, y); principal stress directions (1, 2); and concrete principal coordinate system (r, d) of RC elements.

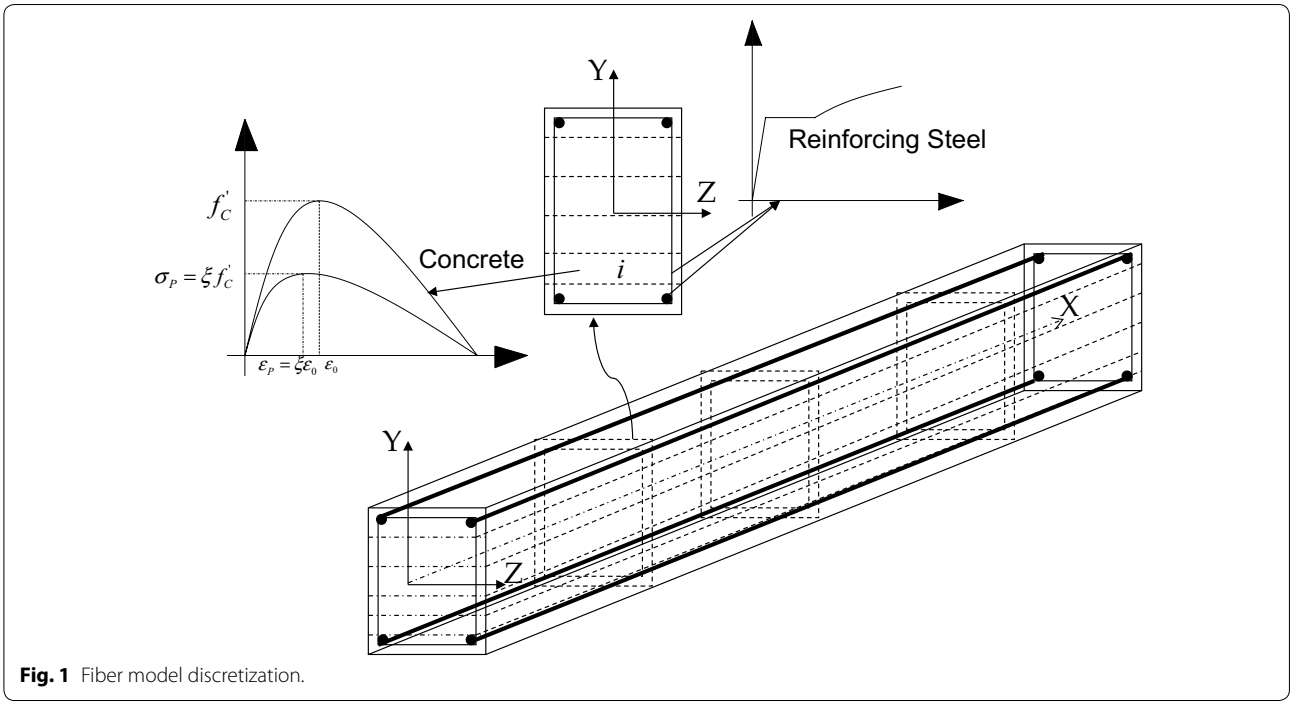

Fig. 1 Fiber model discretization.

To following matrix $R(\theta)$ is used to rotate the stress and strain vectors from one coordinate system to another:

$$[R(\theta)] = \begin{bmatrix} \cos^2\theta & \sin^2\theta & 2\cos\theta\sin\theta \\ \sin^2\theta & \cos^2\theta & -2\cos\theta\sin\theta \\ -\cos\theta\sin\theta & \cos\theta\sin\theta & \cos^2\theta - \sin^2\theta \end{bmatrix} \tag{1}$$

where θ is the angle between the two coordinate systems.

The compatibility equations in the x–y system are:

$$\{\ \varepsilon_x\ \ \varepsilon_y\ \ 0.5\gamma_{xy}\ \}^T = [R(-\alpha_1)]\{\ \varepsilon_1\ \ \varepsilon_2\ \ 0.5\gamma_{12}\ \}^T \tag{2}$$

Similar to the strain transformations, stress transformation equations in the x–y system are:

$$\{\ \sigma_x\ \ \sigma_y\ \ \tau_{xy}\ \}^T = [R(-\alpha_1)]\{\ \sigma_1^c\ \ \sigma_2^c\ \ \tau_{12}^c\ \}^T \tag{3}$$

The transformation equations are graphically represented by Mohr's stress and strain circles in Fig. 3.

For a fiber Timoshenko-type beam element formulation, the state determination at the fiber level uses the strain state $\{\varepsilon_x, \varepsilon_y, \gamma_{xy}\}$ to evaluate the fiber stresses $\{\sigma_x, \sigma_y, \tau_{xy}\}$. In this case, the values of ε_x, γ_{xy} are given, but the lateral strain ε_y value is unknown and has to be calculated from the equilibrium equations as described next.

4 Process to Evaluate Lateral Strains

To evaluate the lateral strain, the equilibrium equations between concrete and steel are given below:

$$\begin{Bmatrix} \sigma_x \\ \sigma_y \\ \tau_{xy} \end{Bmatrix} = \begin{bmatrix} \cos^2\alpha_1 & \sin^2\alpha_1 & -2\cos\alpha_1\sin\alpha_1 \\ \sin^2\alpha_1 & \cos^2\alpha_1 & 2\cos\alpha_1\sin\alpha_1 \\ \cos\alpha_1\sin\alpha_1 & -\cos\alpha_1\sin\alpha_1 & \cos^2\alpha_1 - \sin^2\alpha_1 \end{bmatrix} \begin{Bmatrix} \sigma_1^c \\ \sigma_2^c \\ \tau_{12}^c \end{Bmatrix} + \begin{Bmatrix} \rho_{sx} f_{sx} \\ \rho_{sy} f_{sy} \\ 0 \end{Bmatrix} \tag{4}$$

where f_{sx} and f_{sy} are the reinforcing bar stresses in the x and y directions respectively, and ρ_{sx}, ρ_{sy} are the smeared steel ratios in the x and y directions respectively.

The lateral strain ε_y in fiber i is calculated from the second of Equations in (4), knowing that the value of σ_y equals zero. In order to evaluate the value of the lateral strain ε_y, an iterative procedure is needed owing to the nonlinear behavior of the materials used (Mullapudi and Ayoub 2010).

5 Uni-Axial Constitutive Relationships of the Materials

The biaxial strains in the x–y direction $\{\ \varepsilon_x\ \ \varepsilon_y\ \ \gamma_{xy}\ \}^T$ need to be converted to equivalent uniaxial strains in the principal *1–2* direction $\{\ \bar{\varepsilon}_1\ \ \bar{\varepsilon}_2\ \ \gamma_{12}\ \}^T$ in order to evaluate the concrete stresses as explained in (Mullapudi and Ayoub 2010).

To evaluate the rotating crack angle, α_r corresponding to a concrete shear stress $\tau_{12}^c = 0$ (Fig. 3) the following expression is used:

$$\tan 2\alpha_r = \frac{\gamma_{xy}}{\varepsilon_x - \varepsilon_y} \tag{5}$$

The calculation of the rotating angle, α_r is dependent on the strain state. The calculation of the trial rotating angle, α_r^* from the Mohr circle (Fig. 3) is based on the strain values

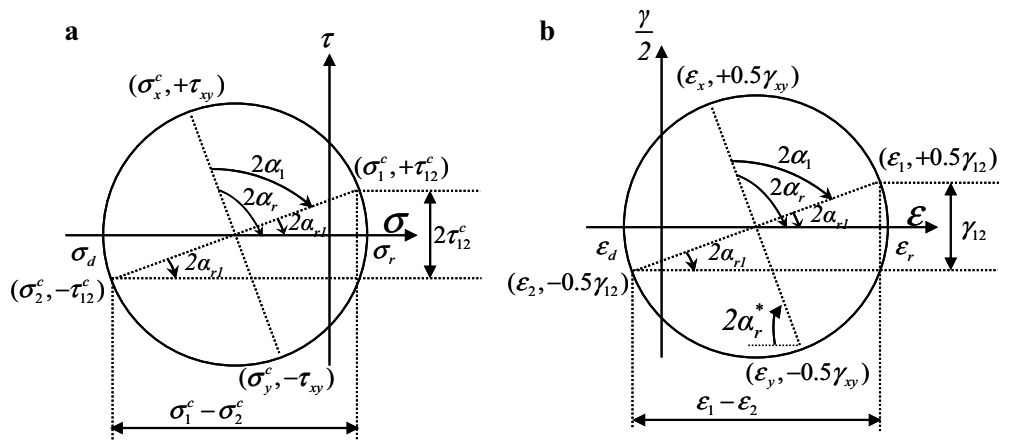

Fig. 3 Mohr Circle representation of stresses and strains **a** Stress, **b** strain.

$$\alpha_r^* = 0.5 \tan^{-1}\left(\left|\frac{\gamma_{xy}}{\varepsilon_x - \varepsilon_y}\right|\right) \tag{6}$$

If the value of the difference between the axial and transverse strains $|\varepsilon_x - \varepsilon_y| = 0$, then the value of the rotating angle α_r depends upon the value of the shear strain γ_{xy} as follows.

Rotating angle $\alpha_r = 45°$ when the value of $\gamma_{xy} > 0$, and $\alpha_r = 135°$ when the value of the $\gamma_{xy} < 0$.

If the value of the shear strain $\gamma_{xy} = 0$ then the rotating angle depends upon the value of the ε_x and ε_y as follows.

The rotating angle $\alpha_r = 0°$ when the value of $\varepsilon_x > \varepsilon_y$ and, $\alpha_r = 90°$ when the value of $\varepsilon_x < \varepsilon_y$.

If both the shear strain and the difference of the axial and transverse strains are non-zero numbers, then the following laws will be applied.

- If the value of $\varepsilon_x > \varepsilon_y$ and the shear strain $\gamma_{xy} > 0$, then the value of the rotating angle α_r becomes the value of the α_r^*.
- If the value of $\varepsilon_x > \varepsilon_y$ and the shear strain $\gamma_{xy} < 0$, then the value of the rotating angle $\alpha_r = 180° - \alpha_r^*$.
- If the value of $\varepsilon_x < \varepsilon_y$ and the shear strain $\gamma_{xy} > 0$, then the value of the rotating angle $\alpha_r = 90° - \alpha_r^*$.
- If the value of $\varepsilon_x < \varepsilon_y$ and the shear strain $\gamma_{xy} < 0$, then the value of the rotating angle $\alpha_r = 90° + \alpha_r^*$.

After evaluating the ε_y term that satisfies the equilibrium condition (Eq. 4), the principal angle α_1 is evaluated as:

$$\tan 2\alpha_1 = \frac{2\tau_{xy}}{\sigma_x - \sigma_y} \tag{7}$$

Similar to Eq. (2), the biaxial principal strains are calculated as follow:

$$\left\{ \varepsilon_1 \;\; \varepsilon_2 \;\; 0.5\gamma_{12} \right\}^T = [R(\alpha_1)] \left\{ \varepsilon_x \;\; \varepsilon_y \;\; 0.5\gamma_{xy} \right\}^T \tag{8}$$

The biaxial strains in the x–y direction $\left\{ \varepsilon_x \;\; \varepsilon_y \;\; \gamma_{xy} \right\}^T$ need to be converted to equivalent uniaxial strains in the principal *1–2* direction $\left\{ \bar{\varepsilon}_1 \;\; \bar{\varepsilon}_2 \;\; \gamma_{12} \right\}^T$ in order to evaluate the concrete stresses as explained in (Mullapudi and Ayoub 2010). This is done using the Hsu/Zhu ratios (μ_{12}, μ_{21}) (Zhu and Hsu 2002). μ_{12} is the ratio of the tensile strain increment in direction *1* to the compressive strain increment in direction *2*, and μ_{21} is the ratio of the compressive strain increment in direction *2* to the tensile strain increment in direction *1*. Based on test data the following expressions are proposed by Zhu and Hsu (2002).

$$\mu_{12} = 0.2 + 850\varepsilon_{sf} \quad \varepsilon_{sf} \le \varepsilon_y, \tag{9}$$

$$\mu_{12} = 1.9 \quad \varepsilon_{sf} > \varepsilon_y \tag{10}$$

where ε_{sf} is the strain in the steel bar that yields first and ε_y is the yield strain.

After cracking, the value of the Hsu/Zhu ratio μ_{12} is larger than maximum value of 0.5 for Poisson ratios of continuous materials. Before cracking, the Hsu/Zhu ratio $\mu_{21} = 0.2$ and, after cracking, $\mu_{21} = 0$, meaning the tensile strain does not affect the compressive strain.

The Hsu/Zhu ratio is used to elate the uni-axial strains to the biaxial principal strains:

$$\left\{ \bar{\varepsilon}_{sx} \;\; \bar{\varepsilon}_{sy} \;\; 0.5\gamma_{xy} \right\}^T = [\mu][R(-\alpha_1)] \left\{ \varepsilon_1 \;\; \varepsilon_2 \;\; 0.5\gamma_{12} \right\}^T \tag{11}$$

where

$$[\mu] = \begin{bmatrix} \frac{1}{1-\mu_{12}\mu_{21}} & \frac{\mu_{12}}{1-\mu_{12}\mu_{21}} & 0 \\ \frac{\mu_{21}}{1-\mu_{12}\mu_{21}} & \frac{1}{1-\mu_{12}\mu_{21}} & 0 \\ 0 & 0 & 1 \end{bmatrix} \tag{12}$$

The longitudinal and transverse reinforcement uniaxial principal strains are then:

$$\bar{\varepsilon}_{sx} = \left(\frac{1}{1-\mu_{12}\mu_{21}}\varepsilon_1 + \frac{\mu_{12}}{1-\mu_{12}\mu_{21}}\varepsilon_2\right)\cos^2(\alpha_1) + \left(\frac{\mu_{21}}{1-\mu_{12}\mu_{21}}\varepsilon_1 + \frac{1}{1-\mu_{12}\mu_{21}}\varepsilon_2\right)\sin^2(\alpha_1) - \gamma_{12}\sin(\alpha_1)\cos(\alpha_1) \tag{13}$$

$$\bar{\varepsilon}_{sy} = \left(\frac{1}{1-\mu_{12}\mu_{21}}\varepsilon_1 + \frac{\mu_{12}}{1-\mu_{12}\mu_{21}}\varepsilon_2\right)\sin^2(\alpha_1) + \left(\frac{\mu_{21}}{1-\mu_{12}\mu_{21}}\varepsilon_1 + \frac{1}{1-\mu_{12}\mu_{21}}\varepsilon_2\right)\cos^2(\alpha_1) +' \gamma_{12}\sin(\alpha_1)\cos(\alpha_1) \tag{14}$$

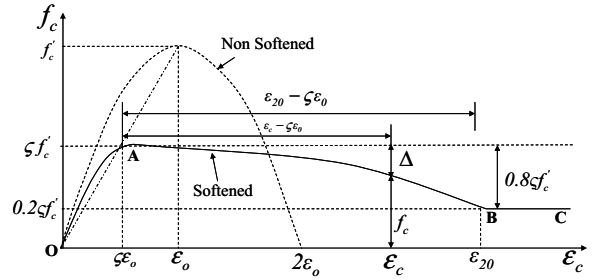

Fig. 4 Monotonic softened concrete material model.

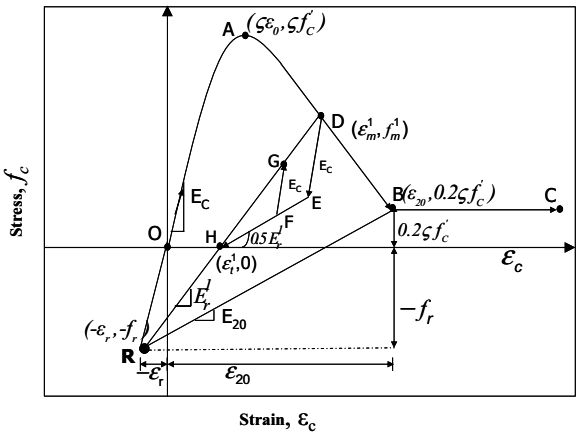

Fig. 5 Cyclic stress–strain curve of softened concrete.

The equivalent uniaxial longitudinal and transverse steel stresses, f_{sx} and f_{sy} respectively are evaluated from the corresponding steel strains $\bar{\varepsilon}_{sx}$ and $\bar{\varepsilon}_{sy}$ through a proper steel constitutive model. The equivalent uniaxial strains $\bar{\varepsilon}_1$ and $\bar{\varepsilon}_2$ are also used to evaluate the concrete stresses σ_1^c and σ_2^c.

5.1 Concrete Model

The uniaxial concrete material model adopted follows the well-established modified Kent and Park model (Park et al. 1982). However, the model was modified to account for the following effects:

- First, the softening effect for both, the stresses and strains, is accounted for.
- Second, the cyclic stiffness degradation for both, the unloading and reloading branches, is introduced.
- Third, the tension-stiffening effect is accounted for (Belarbi and Hsu 1994).

According to Kent and Park (Park et al. 1982), the monotonic stress–strain envelope of concrete follows a parabolic curve (Fig. 4):

$$f_c = f_c^{'}\left[2\left(\frac{\varepsilon_c}{\varepsilon_0}\right) - \left(\frac{\varepsilon_c}{\varepsilon_0}\right)^2\right] \tag{15}$$

It was observed from experimental tests of concrete panels that the compressive stress–strain curve is reduced due to the effect of perpendicular tensile stresses. This effect is accounted for through a softening coefficient ς. When the softened stress–strain curve is developed, it is assumed that the lines that connect the origin to the peak stress of the softened and non-softened curve have the same slope as shown in Fig. 4. Similarly, the pre-peak and post-peak curves of the softened member are assumed to follow a parabolic shape. The descending branch of the softened envelope is gently sloped until the stress reaches a value that equals 20% of the maximum stress $\varsigma f_c'$ at a strain of ε_{20}. The residual concrete compressive strength is assumed to be 20% of the softened concrete compressive strength ($\varsigma f_c'$). The sse of this value in the model is very common and has accurately predicted the experimental results (Mullapudi and Ayoub 2013).

For the softened behavior, the following relationships are adopted:

$$\text{Region OA, } \varepsilon_c \le \varsigma\varepsilon_0, f_c = \varsigma f_c^{'}\left[2\left(\frac{\varepsilon_c}{\varsigma\varepsilon_0}\right) - \left(\frac{\varepsilon_c}{\varsigma\varepsilon_0}\right)^2\right] \tag{16}$$

$$\text{Region OA, } \varepsilon_c \le \varsigma\varepsilon_0, \text{ Tangent modulus } E_t = \frac{2f_c^{'}}{\varepsilon_0}\left(1 - \frac{\varepsilon_c}{\varsigma\varepsilon_0}\right) \tag{17}$$

$$\text{Region AB, } \varsigma\varepsilon_0 < \varepsilon_c \le \varepsilon_{20}, f_c = \varsigma f_c^{'}\left[1 - 0.8\left(\frac{\varepsilon_c - \varsigma\varepsilon_0}{\varepsilon_{20} - \varsigma\varepsilon_0}\right)^2\right] \tag{18}$$

$$\text{Region AB, } \varsigma\varepsilon_0 < \varepsilon_c \le \varepsilon_{20},$$

$$\text{Tangent modulus } E_t = -1.6\varsigma f_c^{'}\left(\frac{\varepsilon_c - \varsigma\varepsilon_0}{(\varepsilon_{20} - \varsigma\varepsilon_0)^2}\right) \tag{19}$$

$$\text{Region BC, } \varepsilon_c > \varepsilon_{20}, f_c = 0.2\varsigma f_c' \tag{20}$$

$$\text{Region BC, } \varepsilon_c > \varepsilon_{20}, \text{ Tangent modulus } E_t = 0. \tag{21}$$

The cyclic model (Fig. 5) considers the concrete damage and accounts for the crack opening and closing. The envelope for the cyclic stress–strain curves of concrete adheres to the monotonic stress–strain curve. The unloading and reloading path of the compressive side is simplified, as all the loading paths start from a common point *R*, which determines the degradation stiffness (i.e. the ratio between the slope of any given loading path and that of the monotonic envelope at the origin), which limit is provided by the slope of the path *RB*.

The unloading modulus E_{20} at point *B* of the monotonic envelope curve is $\frac{0.2\varsigma f_c^{'}-f_r}{\varepsilon_{20}-\varepsilon_r}$. E_{20} and must be determined experimentally. The stress and strain at the intersection of point *R* and the origin are given by the following expressions:

$$\varepsilon_r = \frac{0.2\varsigma f_c^{'} - E_{20}\varepsilon_{20}}{E_c - E_{20}} \tag{22}$$

$$f_r = E_c\varepsilon_r \tag{23}$$

in which E_c is the initial tangent modulus at origin in compression; in the current model, it is assumed to equal $\frac{2f_c^{'}}{\varepsilon_0}$. The unloading stress f_m^1 and strain ε_m^1 values at point *D* on the compressive monotonic envelope are used to calculate the reloading modulus and strain ε_t^1 at zero stress point *H* from the following expressions:

$$E_r^1 = \frac{f_m - f_r}{\varepsilon_m - \varepsilon_r} \tag{24}$$

$$\varepsilon_t^1 = \varepsilon_m^1 - \frac{f_m^1}{E_r^1} \tag{25}$$

From any unloading point *D*, the stress will reach the zero stress axis at point *H* after completing two smaller cycles that are defined by these expressions:

$$\text{Maximum stress (line HD) } f_{max}^1 = f_m^1 + E_r^1\left(\varepsilon_c - \varepsilon_m^1\right),\ \varepsilon_t^1 \le \varepsilon_c \le \varepsilon_m^1 \tag{26}$$

$$\text{Minimum stress (line HE) } f_{min}^1 = 0.5E_r^1\left(\varepsilon_c - \varepsilon_t^1\right),\ \varepsilon_t^1 \le \varepsilon_c \le \varepsilon_m^1. \tag{27}$$

The loading and unloading cycles are carried out with the assumption that the model follows a linear behavior with modulus E_c. The trial stress f_c^T and tangent modulus E_t are based on a linear elastic behavior with initial tangent modulus E_c; later this assumption is corrected to fall under the line *HD* and line *HE*.

$$f_c^T = f_c^P + E_c\Delta\varepsilon_c \tag{28}$$

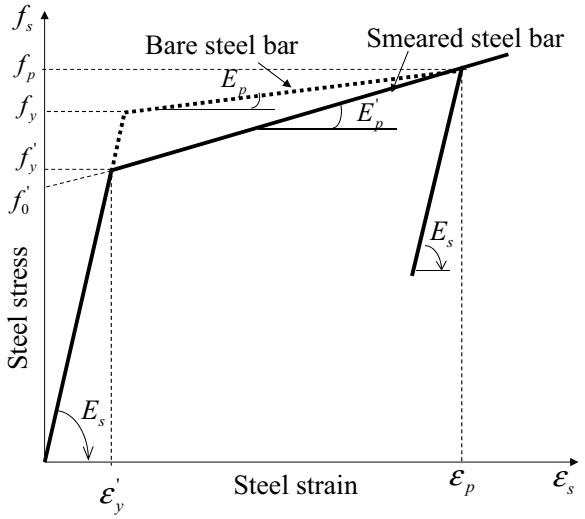

Fig. 6 Smeared mild steel stress–strain curve.

Here, f_c^P is the previous stress and $\Delta\varepsilon_c$ is the strain increment.

The actual stress f_c and tangent modulus E_t are calculated based on the trial stress state

$$f_{min}^1 \le f_c^T \le f_{max}^1 \text{ then } f_c = f_c^T \text{ and } E_t = E_c \tag{29}$$

$$f_c^T < f_{min}^1 \text{ then } f_c = f_{min}^1 \text{ and } E_t = 0.5E_r^1 \tag{30}$$

$$f_c^T > f_{max}^1 \text{ then } f_c = f_{max}^1 \text{ and } E_t = E_r^1. \tag{31}$$

When the unloading begins from points *D* to E, the reloading will follow the same path back to *D*. When the unloading reaches point *F,* then reloading will result in the loop *DEFGD*. If unloading reaches point *H,* then reloading will follow loop *DEHD*. The reloading path will always rejoin the compression envelope at the point of initial unloading, *D*. If unloading continues below point *H,* then reloading begins in tension. After the start of the reloading in compression, the model will re-enter the compression branch at point *H*. Subsequent loading in the tension branch will not affect the behavior once the model returns back to the compression branch.

5.2 Steel Model

The smeared stress–strain relationship of steel embedded in concrete under uni-axial loading has been developed by Belarbi and Hsu (1994, 1995). The steel strain at cracked sections typically increases rapidly compared to adjacent regions because part of the stress is resisted by the concrete. Steel stresses are averaged along the reinforcing bar crossing several cracks, and the resulting smeared steel stress at first yield is reduced compared to the local yield stress of a bare bar. The smeared

stress–strain relationship of embedded steel bars (solid curves), as well as that of bare bar (dotted curve) are plotted in Fig. 6.

The difference between the bare bar yield stress f_y and smeared steel bar yield stress f_y' depends on the parameter B defined by Belarbi and Hsu (1994, 1995). The parameter $B$is derived to be a function of three variables such as percentage of steel (ρ), cracking strength of concrete (f_{cr}), and yield stress of the bare bar (f_y). The parameter B depends on the crack width, crack spacing and interface bond slip behavior of steel bar and concrete. It can be seen that when the steel ratio ρ is decreased or when f_{cr} is increased, then the smeared yield stress f_y' decreases and the smeared stress–strain plot moves downward.

As shown in Fig. 6, the shape of both, the bare bar and the smeared steel bar, curves of mild steel follow two straight lines. These two straight lines have slopes of E_s before yielding and E_p' after yielding for smeared steel, and slope of E_p after yielding for bare steel bar as illustrated in Fig. 6. The slope of the strain-hardening branch of the bare steel bar is assumed to equal 0.025 E_s. The stress value at which the two straight lines of smeared steel intersect is the smeared yield stress f_y' and the corresponding strain is the smeared yield strain ε_y'.

The equations of the pre yield and post yield lines are given as:

$$f_s = E_s\varepsilon_s \quad \text{when} \quad f_s \le f_y^{'} \tag{32}$$

$$f_s = f_o^{'} + E_p^{'}\varepsilon_s \quad \text{when} \quad f_s > f_y^{'}. \tag{33}$$

The vertical intercept of the post yield line f_o' is evaluated as:

$$f_o^{'} = \frac{E_s - E_p^{'}}{E_s} f_y^{'} \tag{34}$$

Belarbi and Hsu (1994, 1995) defined the parameter Bas:

$$\mathrm{B} = \frac{1}{\rho}\left(\frac{f_{cr}}{f_y}\right)^{1.5}, \tag{35}$$

where $f_{cr} = 0.31\sqrt{f_c^{'}(MPa)}$ and $\rho \ge 0.15\%$.

The smeared yield stress of steel bar is calculated as:

$$f_y^{'} = (0.93 - 2\mathrm{B})f_y \tag{36}$$

The smeared steel bar yield strain is calculated as:

$$\varepsilon_y^{'} = \frac{f_y^{'}}{E_s}. \tag{37}$$

The slope of the strain hardening branch of the smeared steel bar is calculated as

$$E_p^{'} = 0.02 + B. \tag{38}$$

The smeared steel stress before yielding can be calculated as:

$$f_s = E_s \quad \text{when}\ \varepsilon_s \le \varepsilon_y^{'} \tag{39}$$

$$f_s = (0.91 - 2\mathrm{B})f_y + (0.02 + 0.25\mathrm{B})E_s\bar{\varepsilon}_s \quad \text{when}\ \varepsilon_s > \varepsilon_y^{'}. \tag{40}$$

When the steel stress f_s reaches a value of f_p and begins to unload, then the unloading branch follows a straight line with a slope of E_s. The unloading stress is expressed as:

$$f_s = f_p - E_s(\varepsilon_p - \varepsilon_s) \quad \text{where}\ \varepsilon_s < \varepsilon_p \tag{41}$$

The cyclic response of the smeared steel bar is formulated according to the Filippou et al. (1983) model which accounts for isotropic strain hardening and Bauschinger effect.

6 Tangent Material Constitutive Relations

The concrete constitutive law is simplified as an orthotropic material with two perpendicular planes of elastic symmetry. Directions one and two are the local principal material axes that are normal to the planes of symmetry. With the equivalent uni-axial strains, the stiffness values $\bar{E}_1^c$ and $\bar{E}_2^c$ are determined from a material uni-axial stress–strain relationship. The material behavior is expressed as:

$$\{\sigma_{12}^c\} = [D_{lo}]^c\{\varepsilon_{12}\} \tag{42}$$

In this equation, $\{\sigma_{12}^c\}$ is the concrete stress vector, $\{\varepsilon_{12}\}$ is the principal strain vector, and $[D_{lo}]^c$ is the principal local uni-axial concrete material tangent stiffness matrix.

The tangent stiffness matrix of an RC element is defined as:

$$[D_{gl}]^{c+s} = \frac{d\begin{Bmatrix}\sigma_x\\ \sigma_y\\ \tau_{xy}\end{Bmatrix}}{d\begin{Bmatrix}\varepsilon_x\\ \varepsilon_y\\ \frac{1}{2}\gamma_{xy}\end{Bmatrix}}, \tag{43}$$

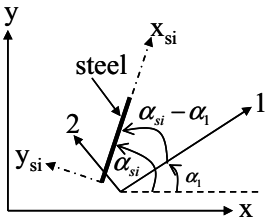

Fig. 7 Coordinate system for reinforced concrete element.

$$\begin{Bmatrix} \sigma_x \\ \sigma_y \\ \tau_{xy} \end{Bmatrix} = [R(-\alpha_1)] \begin{Bmatrix} \sigma_1^c \\ \sigma_2^c \\ \tau_{12}^c \end{Bmatrix} + \sum_i [R(-\alpha_{si})] \begin{Bmatrix} \rho_{si} f_{si} \\ 0 \\ 0 \end{Bmatrix}, \tag{44}$$

where ρ_{si} is the reinforcement ratio in the ith direction; and $[R(-\alpha_1)]$ and $[R(-\alpha_{si})]$ are the transformation matrices from the local 1–2 coordinate and the $x_{si}-y_{si}$ reinforcement coordinate system, to the x–y coordinate system, respectively (Fig. 7).

Substituting Eq. (44) into Eq. (43) gives:

$$[D_{gl}]^{c+s} = \frac{\partial \left([R(-\alpha_1)] \begin{Bmatrix} \sigma_1^c \\ \sigma_2^c \\ \tau_{12}^c \end{Bmatrix} + \sum_i [R(-\alpha_{si})] \begin{Bmatrix} \rho_{si} f_{si} \\ 0 \\ 0 \end{Bmatrix} \right)}{\partial \begin{Bmatrix} \varepsilon_x \\ \varepsilon_y \\ \frac{1}{2}\gamma_{xy} \end{Bmatrix}}. \tag{45}$$

Equation (45) is split into a concrete stiffness $[D_{gl}]^c$ and a reinforcement stiffness $[D_{gl}]^s$ as:

$$[D_{gl}]^c = \frac{\partial \left([R(-\alpha_1)] \begin{Bmatrix} \sigma_1^c \\ \sigma_2^c \\ \tau_{12}^c \end{Bmatrix} \right)}{\partial \begin{Bmatrix} \varepsilon_x \\ \varepsilon_y \\ \frac{1}{2}\gamma_{xy} \end{Bmatrix}}, \tag{46}$$

and

$$[D_{gl}]^s = \frac{\partial \left(\sum_i [R(-\alpha_{si})] \begin{Bmatrix} \rho_{si} f_{si} \\ 0 \\ 0 \end{Bmatrix} \right)}{\partial \begin{Bmatrix} \varepsilon_x \\ \varepsilon_y \\ \frac{1}{2}\gamma_{xy} \end{Bmatrix}}. \tag{47}$$

Thus the total stiffness becomes:

$$[D_{gl}]^{c+s} = [D_{gl}]^c + [D_{gl}]^s, \tag{48}$$

where $[D_{gl}]^c$ is the tangent material constitutive matrix of concrete; and $[D_{gl}]^s$ is the tangent material constitutive matrix of the steel bars.

The equivalent uni-axial strains can be calculated from the global strains using:

$$\begin{Bmatrix} \bar{\varepsilon}_1 \\ \bar{\varepsilon}_2 \\ \frac{1}{2}\gamma_{12} \end{Bmatrix} = [\mu] \cdot [R(\alpha_1)] \cdot \begin{Bmatrix} \varepsilon_x \\ \varepsilon_y \\ \frac{1}{2}\gamma_{xy} \end{Bmatrix}, \tag{49}$$

where $[\mu]$ is the Hsu/Zhu ratio matrix as shown in Eq. 12.

After substituting Eq. (49) into Eq. (46):

$$[D_{gl}]^c = [R(-\alpha_1)] \cdot \begin{bmatrix} \frac{\partial \sigma_1^c}{\partial \bar{\varepsilon}_1} & \frac{\partial \sigma_1^c}{\partial \bar{\varepsilon}_2} & \frac{\partial \sigma_1^c}{\partial \left(\frac{1}{2}\gamma_{12}\right)} \\ \frac{\partial \sigma_2^c}{\partial \bar{\varepsilon}_1} & \frac{\partial \sigma_2^c}{\partial \bar{\varepsilon}_2} & \frac{\partial \sigma_2^c}{\partial \left(\frac{1}{2}\gamma_{12}\right)} \\ \frac{\partial \tau_{12}^c}{\partial \bar{\varepsilon}_1} & \frac{\partial \tau_{12}^c}{\partial \bar{\varepsilon}_2} & \frac{\partial \tau_{12}^c}{\partial \left(\frac{1}{2}\gamma_{12}\right)} \end{bmatrix} \cdot [\mu] \cdot [R(\alpha_1)]. \tag{50}$$

From Eq. (50), the concrete local tangential stiffness can be written as:

$$[D_{lo}]^c = \begin{bmatrix} \frac{\partial \sigma_1^c}{\partial \bar{\varepsilon}_1} & \frac{\partial \sigma_1^c}{\partial \bar{\varepsilon}_2} & \frac{\partial \sigma_1^c}{\partial \left(\frac{1}{2}\gamma_{12}\right)} \\ \frac{\partial \sigma_2^c}{\partial \bar{\varepsilon}_1} & \frac{\partial \sigma_2^c}{\partial \bar{\varepsilon}_2} & \frac{\partial \sigma_2^c}{\partial \left(\frac{1}{2}\gamma_{12}\right)} \\ \frac{\partial \tau_{12}^c}{\partial \bar{\varepsilon}_1} & \frac{\partial \tau_{12}^c}{\partial \bar{\varepsilon}_2} & \frac{\partial \tau_{12}^c}{\partial \left(\frac{1}{2}\gamma_{12}\right)} \end{bmatrix}. \tag{51}$$

After substituting Eq. (51) into Eq. (50):

$$[D_{gl}]^c = [R(-\alpha_1)] \cdot [D_{lo}]^c \cdot [\mu] \cdot [R(\alpha_1)]. \tag{52}$$

The diagonal terms in Eq. (64) matrix can be found directly from the uni-axial stresses and strains in the respective directions. The first diagonal term $\frac{\partial \sigma_1^c}{\partial \bar{\varepsilon}_1} = \bar{E}_1^c$ is the tangential uni-axial modulus of concrete in the 1-direction, the second diagonal term $\frac{\partial \sigma_2^c}{\partial \bar{\varepsilon}_2} = \bar{E}_2^c$ is the tangential uni-axial modulus of concrete in the 2-direction, and the third diagonal term $\frac{\partial \tau_{12}^c}{\partial \left(\frac{1}{2}\gamma_{12}\right)} = \frac{\sigma_1^c - \sigma_2^c}{\varepsilon_1 - \varepsilon_2} = G_{12}^c$ is the shear modulus. The off-diagonal terms $\frac{\partial \sigma_1^c}{\partial \bar{\varepsilon}_2}$ and $\frac{\partial \sigma_2^c}{\partial \bar{\varepsilon}_1}$ are obtained using the uni-axial stresses and the uni-axial strains in the orthogonal direction. These off-diagonal terms are not zero because the stress and strains of the concrete in compression is softened by the perpendicular tensile strains.

Therefore, $[D_{lo}]^c$ can be written as:

$$[D_{lo}]^c = \begin{bmatrix} \bar{E}_1^c & \frac{\partial \sigma_1^c}{\partial \bar{\varepsilon}_2} & 0 \\ \frac{\partial \sigma_2^c}{\partial \bar{\varepsilon}_1} & \bar{E}_2^c & 0 \\ 0 & 0 & G_{12}^c \end{bmatrix}. \tag{53}$$

The off-diagonal terms can be determined with three cases as described below.

6.1 Equivalent uni-axial strains $\bar{\varepsilon}_1 > 0$ and $\bar{\varepsilon}_2 > 0$

When $\bar{\varepsilon}_1 > 0$ and $\bar{\varepsilon}_2 > 0$ then the uni-axial concrete stresses σ_1^c and σ_2^c are calculated only from uni-axial strains $\bar{\varepsilon}_1$ and $\bar{\varepsilon}_2$, respectively.

Therefore,

$$\frac{\partial \sigma_1^C}{\partial \bar{\varepsilon}_2} = 0 \quad \text{and} \quad \frac{\partial \sigma_2^C}{\partial \bar{\varepsilon}_1} = 0. \tag{54}$$

6.2 Equivalent uni-axial strains $\bar{\varepsilon}_1 > 0$ and $\bar{\varepsilon}_2 < 0$

When the uni-axial strain is $\bar{\varepsilon}_1 > 0$ then the uni-axial compressive stress σ_1^c is calculated directly from the $\bar{\varepsilon}_1$, and σ_1^c is not a function of the orthogonal concrete strain $\bar{\varepsilon}_2$. Therefore, $\frac{\partial \sigma_1^C}{\partial \bar{\varepsilon}_2} = 0$.

To obtain $\frac{\partial \sigma_2^C}{\partial \bar{\varepsilon}_1}$, the constitutive law of the concrete strut in compression is needed.

In order to obtain $\frac{\partial \sigma_2^C}{\partial \bar{\varepsilon}_1}$, the constitutive law of concrete in compression is needed.

$$\sigma_2^C = \zeta \cdot f_C^{'} \cdot \left[2\left(\frac{\bar{\varepsilon}_2}{\zeta \varepsilon_0}\right) - \left(\frac{\bar{\varepsilon}_2}{\zeta \varepsilon_0}\right)^2 \right], \quad \frac{\bar{\varepsilon}_2}{\zeta \varepsilon_0} \leq 1, \tag{55}$$

$$\sigma_2^C = \zeta \cdot f_C^{'} \cdot \left[1 - \left(\frac{\bar{\varepsilon}_2/(\zeta \varepsilon_0) - 1}{4/\zeta - 1}\right)^2 \right], \quad \frac{\bar{\varepsilon}_2}{\zeta \varepsilon_0} > 1, \tag{56}$$

where the softening coefficient ζ (Hsu and Zhu 2002)

$$\zeta = \left(\frac{5.8}{\sqrt{f_c^{'}(MPa)}} \leq 0.9\right)\left(\frac{1}{\sqrt{1+400\bar{\varepsilon}_1}}\right)\left(1 - \frac{|\alpha_{r1}^0|}{24^0}\right). \tag{57}$$

In Eq. (57), α_{r1} is in degrees. If the value of the α_{r1} is in radians then the value of the 24° should be converted into radians. From panel tests up to 100 MPa of concrete compressive strength, the deviation angle α_{r1} is equal to or less than 24° (Wang 2006)

After making the required changes, Eq. (57) becomes

$$\zeta = \left(\frac{5.8}{\sqrt{f_c^{'}(MPa)}} \leq 0.9\right)\left(\frac{1}{\sqrt{1+400\bar{\varepsilon}_1}}\right)\left(1 - \frac{15|\alpha_{r1}^c|}{2\pi}\right), \tag{58}$$

$$\alpha_{r1}^c = 0.5 \tan^{-1}\left(\frac{\gamma_{12}}{\varepsilon_1 - \varepsilon_2}\right) \text{ and} \tag{59}$$

$$\varepsilon_1 = \bar{\varepsilon}_1 - \mu_{12}\bar{\varepsilon}_2 \quad \text{and} \quad \varepsilon_2 = \bar{\varepsilon}_2 - \mu_{21}\bar{\varepsilon}_1, \tag{60}$$

where ε_1 and ε_2 are the biaxial strains in the 1–2 coordinate system and $\bar{\varepsilon}_1$ and $\bar{\varepsilon}_2$ are the equivalent uni-axial strains in the 1–2 coordinate system.

From Eqs. 59 and 60:

$$\alpha_{r1}^c = 0.5 \tan^{-1}\left(\frac{\gamma_{12}}{\bar{\varepsilon}_1(1+\mu_{21}) - \bar{\varepsilon}_2(1+\mu_{12})}\right), \tag{61}$$

where μ_{12} and μ_{21} are the Hsu/Zhu ratios (Zhu and Hsu 2002)

$\frac{\partial \sigma_2^C}{\partial \bar{\varepsilon}_1}$ can be written as $\frac{\partial \sigma_2^C}{\partial \bar{\varepsilon}_1} = \frac{\partial \sigma_2^C}{\partial \zeta} \cdot \frac{\partial \zeta}{\partial \bar{\varepsilon}_1}$. (62)

$\frac{\partial \zeta}{\partial \bar{\varepsilon}_1}$ can be derived after substituting Eq. (61) into Eq. (58):

$$\frac{\partial \zeta}{\partial \bar{\varepsilon}_1} = \frac{\partial\left(\left(\frac{5.8}{\sqrt{f_c^{'}(\mathrm{MPa})}}\right)\left(\frac{1}{\sqrt{1+400\bar{\varepsilon}_1}}\right)\left(1 - \frac{15}{4\pi}\tan^{-1}\left(\frac{\gamma_{12}}{\bar{\varepsilon}_1(1+\mu_{21}) - \bar{\varepsilon}_2(1+\mu_{12})}\right)\right)\right)}{\partial \bar{\varepsilon}_1} \tag{63}$$

$$= \left(\frac{5.8}{\sqrt{f_c^{'}(\mathrm{MPa})}}\right)\left[\frac{-200}{(1+400\bar{\varepsilon}_1)^{1.5}} + \frac{15}{4\pi}\left(\frac{200\tan^{-1}\left(\frac{\gamma_{12}}{\bar{\varepsilon}_1(1+\mu_{21}) - \bar{\varepsilon}_2(1+\mu_{12})}\right)}{(1+400\bar{\varepsilon}_1)^{1.5}} + \frac{\gamma_{12}(1+\mu_{21})}{(1+400\bar{\varepsilon}_1)^{0.5}\left(\frac{\gamma_{12}}{\bar{\varepsilon}_1(1+\mu_{21}) - \bar{\varepsilon}_2(1+\mu_{12})}\right)^2\left(1 + \frac{(\gamma_{12})^2}{(\bar{\varepsilon}_1(1+\mu_{21}) - \bar{\varepsilon}_2(1+\mu_{12}))^2}\right)}\right)\right] \tag{64}$$

where $\frac{\partial \sigma_2^C}{\partial \zeta}$ can be derived as follow when $\frac{\bar{\varepsilon}_2}{\zeta \varepsilon_0} \leq 1$:

$$\frac{\partial \sigma_2^C}{\partial \zeta} = \frac{\partial \left(\zeta \cdot f_C^{'} \cdot \left[2\left(\frac{\bar{\varepsilon}_2}{\zeta \varepsilon_0} \right) - \left(\frac{\bar{\varepsilon}_2}{\zeta \varepsilon_0} \right)^2 \right] \right)}{\partial \zeta}$$

$$= f_C^{'} \cdot \frac{\partial \left(2\left(\frac{\bar{\varepsilon}_2}{\varepsilon_0} \right) - \frac{(\bar{\varepsilon}_2)^2}{\zeta \varepsilon_0^2} \right)}{\partial \zeta} \tag{65}$$

$$= -f_C^{'} \cdot \frac{(\bar{\varepsilon}_2)^2}{\varepsilon_0^2} \cdot \frac{\partial \left(\frac{1}{\zeta} \right)}{\partial \zeta}$$

$$= -f_C^{'} \cdot \frac{(\bar{\varepsilon}_2)^2}{\varepsilon_0^2} \cdot \left(-\frac{1}{\zeta^2} \right)$$

$$= f_C^{'} \cdot \left(\frac{\bar{\varepsilon}_2}{\zeta \varepsilon_0} \right)^2 \tag{66}$$

when $\frac{\bar{\varepsilon}_2}{\zeta \varepsilon_0} > 1$:

$$\frac{\partial \sigma_2^C}{\partial \zeta} = \frac{\partial}{\partial \zeta} \left(\zeta \cdot f_C^{'} \cdot \left[1 - \left(\frac{\bar{\varepsilon}_2 / (\zeta \varepsilon_0) - 1}{4/\zeta - 1} \right)^2 \right] \right) \tag{67}$$

$$= f_C^{'} \cdot \left(1 - \frac{\partial}{\partial \zeta} \left(\zeta \cdot \left(\frac{\bar{\varepsilon}_2 / (\zeta \varepsilon_0) - 1}{4/\zeta - 1} \right)^2 \right) \right). \tag{68}$$

Let

$$\frac{\partial}{\partial \zeta} \left(\zeta \cdot \left(\frac{\bar{\varepsilon}_2 / (\zeta \varepsilon_0) - 1}{4/\zeta - 1} \right)^2 \right) = A, \tag{69}$$

Equation (67) can be written as:

$$\frac{\partial \sigma_2^C}{\partial \zeta} = f_C^{'} \cdot (1 - A), \tag{70}$$

where

$$A = \left(\frac{\bar{\varepsilon}_2 / (\zeta \varepsilon_0) - 1}{4/\zeta - 1} \right)^2 + \zeta \cdot 2 \cdot \left(\frac{\bar{\varepsilon}_2 / (\zeta \varepsilon_0) - 1}{4/\zeta - 1} \right) \cdot \frac{\partial}{\partial \zeta} \left(\frac{\bar{\varepsilon}_2 / (\zeta \varepsilon_0) - 1}{4/\zeta - 1} \right). \tag{71}$$

Let

$$B = \frac{\partial}{\partial \zeta} \left(\frac{\bar{\varepsilon}_2 / (\zeta \varepsilon_0) - 1}{4/\zeta - 1} \right), \tag{72}$$

Equation (71) can be written as:

$$A = \left(\frac{\bar{\varepsilon}_2 / (\zeta \varepsilon_0) - 1}{4/\zeta - 1} \right)^2 + \zeta \cdot 2 \cdot \left(\frac{\bar{\varepsilon}_2 / (\zeta \varepsilon_0) - 1}{4/\zeta - 1} \right) \cdot B, \tag{73}$$

where

$$B = \frac{\partial}{\partial \zeta} \left(\frac{\bar{\varepsilon}_2 / (\zeta \varepsilon_0) - 1}{4/\zeta - 1} \right) = \frac{\bar{\varepsilon}_2 / \varepsilon_0 - 4}{(4 - \zeta)^2}. \tag{74}$$

Substituting Eq. (74) into Eq. (73) gives:

$$A = \frac{\bar{\varepsilon}_2 / (\zeta \varepsilon_0) - 1}{(4/\zeta - 1)^3} \cdot \left(1 - 12/\zeta + (4/\zeta + 1) \frac{\bar{\varepsilon}_2}{\zeta \varepsilon_0} \right), \left(\frac{\bar{\varepsilon}_2}{\zeta \varepsilon_0} > 1 \right). \tag{75}$$

Substituting Eq. (75) into Eq. (70) gives:

$$\frac{\partial \sigma_2^C}{\partial \zeta} = f_C^{'} \cdot \left(1 - \frac{\bar{\varepsilon}_2 / (\zeta \varepsilon_0) - 1}{(4/\zeta - 1)^3} \cdot \left(1 - 12/\zeta + (4/\zeta + 1) \frac{\bar{\varepsilon}_2}{\zeta \varepsilon_0} \right) \right). \tag{76}$$

Substituting Eqs. (66) and (64) into Eq. (62) gives:When

$$\frac{\bar{\varepsilon}_2}{\zeta \varepsilon_0} \leq 1, \frac{\partial \sigma_2^C}{\partial \bar{\varepsilon}_1} = f_C^{'} \cdot \left(\frac{\bar{\varepsilon}_2}{\zeta \varepsilon_0} \right)^2 \cdot \frac{\partial \zeta}{\partial \bar{\varepsilon}_1}. \tag{77}$$

Substituting Eqs. (76) and (64) into Eq. (62) gives:When

$$\frac{\bar{\varepsilon}_2}{\zeta \varepsilon_0} > 1, \frac{\partial \sigma_2^C}{\partial \bar{\varepsilon}_1} = f_C^{'} \cdot \left(1 - \frac{\bar{\varepsilon}_2 / (\zeta \varepsilon_0) - 1}{(4/\zeta - 1)^3} \cdot \left(1 - 12/\zeta + (4/\zeta + 1) \frac{\bar{\varepsilon}_2}{\zeta \varepsilon_0} \right) \right) \cdot \frac{\partial \zeta}{\partial \bar{\varepsilon}_1}. \tag{78}$$

When the equivalent uni-axial strains $\bar{\varepsilon}_1 < 0$ and $\bar{\varepsilon}_2 > 0$, then the same procedure should be followed.

6.3 Equivalent uni-axial strains $\bar{\varepsilon}_1 < 0$ and $\bar{\varepsilon}_2 < 0$

When $\bar{\varepsilon}_1 < 0$ and $\bar{\varepsilon}_2 < 0$ then concrete will not soften; instead it increases its compressive strength in one direction depending on the confining stress in the orthogonal direction. Because of this reason, the value

of ζ should be greater than or equal to 1. The current research uses the Vecchio's (Vecchio 1992) simplified version of Kupfer et al. (1969) biaxial compression strength envelope. These equations are strength-based; strain-based equations are not available in the literature and need to be investigated in future. Accordingly:

$$\frac{\partial \zeta}{\partial \bar{\varepsilon}_1} = 0 \quad \text{and} \quad \frac{\partial \zeta}{\partial \bar{\varepsilon}_2} = 0 \tag{79}$$

$$\frac{\partial \sigma_1^C}{\partial \bar{\varepsilon}_2} = \frac{\partial \sigma_1^C}{\partial \zeta} \cdot \frac{\partial \zeta}{\partial \bar{\varepsilon}_2} = 0 \tag{80}$$

$$\frac{\partial \sigma_2^C}{\partial \bar{\varepsilon}_1} = \frac{\partial \sigma_2^C}{\partial \zeta} \cdot \frac{\partial \zeta}{\partial \bar{\varepsilon}_1} = 0 \tag{81}$$

The global tangential constitutive matrix of steel $[D_{gl}]^s$can be derived From Fig. 7 as:

$$\begin{Bmatrix} \varepsilon_x \\ \varepsilon_y \\ \frac{1}{2}\gamma_{xy} \end{Bmatrix} = [R(\alpha_1)]^{-1} \cdot [\mu]^{-1} \cdot [R(\alpha_{si} - \alpha_1)]^{-1} \begin{Bmatrix} \bar{\varepsilon}_{si} \\ \bar{\varepsilon}_{si*} \\ \frac{1}{2}\gamma_{si} \end{Bmatrix}. \tag{82}$$

where $\bar{\varepsilon}_{si}$ is the equivalent uni-axial longitudinal strain of the reinforcement, $\bar{\varepsilon}_{si*}$ is the equivalent uni-axial transverse or dowel strain of the reinforcement and γ_{si} is the equivalent uni-axial shear strain of the reinforcement.

Substituting Eq. (82) into Eq. (47) gives:

$$[D_{gl}]^s = \frac{\partial \left(\sum_i [R(-\alpha_{si})] \begin{Bmatrix} \rho_{si} f_{si} \\ 0 \\ 0 \end{Bmatrix} \right)}{\partial \left([R(\alpha_1)]^{-1} \cdot [\mu]^{-1} \cdot [R(\alpha_{si} - \alpha_1)]^{-1} \begin{Bmatrix} \bar{\varepsilon}_{si} \\ \bar{\varepsilon}_{si*} \\ \frac{1}{2}\gamma_{si} \end{Bmatrix} \right)}, \tag{83}$$

$$= \frac{\sum_i [R(-\alpha_{si})] \cdot \rho_{si} \cdot \begin{bmatrix} \frac{\partial f_{si}}{\partial \bar{\varepsilon}_{si}} & \frac{\partial f_{si}}{\partial \bar{\varepsilon}_{si*}} & \frac{\partial f_{si}}{\partial \left(\frac{1}{2}\gamma_{si}\right)} \\ 0 & 0 & 0 \\ 0 & 0 & 0 \end{bmatrix}}{[R(\alpha_1)]^{-1} \cdot [\mu]^{-1} \cdot [R(\alpha_{si} - \alpha_1)]^{-1}}, \tag{84}$$

$$= \sum_i [R(-\alpha_{si})] \cdot \rho_{si} \cdot \begin{bmatrix} \frac{\partial f_{si}}{\partial \bar{\varepsilon}_{si}} & \frac{\partial f_{si}}{\partial \bar{\varepsilon}_{si*}} & \frac{\partial f_{si}}{\partial \left(\frac{1}{2}\gamma_{si}\right)} \\ 0 & 0 & 0 \\ 0 & 0 & 0 \end{bmatrix} [R(\alpha_{si} - \alpha_1)] \cdot [\mu] \cdot [R(\alpha_1)], \tag{85}$$

Let

$$[D_{lo}]^s = \rho_{si} \cdot \begin{bmatrix} \frac{\partial f_{si}}{\partial \bar{\varepsilon}_{si}} & \frac{\partial f_{si}}{\partial \bar{\varepsilon}_{si*}} & \frac{\partial f_{si}}{\partial \left(\frac{1}{2}\gamma_{si}\right)} \\ 0 & 0 & 0 \\ 0 & 0 & 0 \end{bmatrix}, \tag{86}$$

where $\frac{\partial f_{si}}{\partial \bar{\varepsilon}_{si}} = \bar{E}_{si}$, which is the equivalent uni-axial tangential modulus in the longitudinal direction of the reinforcement. The dowel action of the reinforcement is neglected, thus $\frac{\partial f_{si}}{\partial \bar{\varepsilon}_{si*}} = 0$, and also the shear deformation in the reinforcing bar is neglected, thus $\frac{\partial f_{si}}{\partial \left(\frac{1}{2}\gamma_{si}\right)} = 0$.

With these simplifications Eq. (86) can be written as:

$$[D_{lo}]^s = \begin{bmatrix} \rho_{si} \cdot \bar{E}_{si} & 0 & 0 \\ 0 & 0 & 0 \\ 0 & 0 & 0 \end{bmatrix}. \tag{87}$$

Equation (85) can be written as:

$$[D_{gl}]^s = \sum_i [R(-\alpha_{si})] \cdot [D_{lo}]^s \cdot [R(\alpha_{si} - \alpha_1)] \cdot [\mu] \cdot [R(\alpha_1)]. \tag{88}$$

After substituting Eqs. (88) and (51) into Eq. (48) the global tangent material constitutive matrix $[D_{gl}]^{c+s}$ can be evaluated as:

$$\begin{aligned} k_{fiber} = [D_{gl}]^{c+s} &= [R(-\alpha_1)] \cdot [D_{lo}]^c \cdot [\mu] \\ &\cdot [R(\alpha_1)] + \sum_i [T(-\alpha_{si})] \\ &\cdot [D_{lo}]^s \cdot [R(\alpha_{si} - \alpha_1)] \cdot [\mu] \cdot [R(\alpha_1)] \end{aligned} \tag{89}$$

The total section stiffness is evaluated from the sum of concrete and steel stiffness:

$$[K_{Section}] = \sum_1^n k_{fiber}, \tag{90}$$

The total section force is evaluated from the sum of concrete and steel forces in their respective directions:

$$\{F_{Section}\} = \sum_1^n F_{fiber}. \tag{91}$$

where n is the number of concrete and steel fibers in a section.

The element stiffness and forces are calculated with numerical integration of section stiffness and section forces at different section points along the length of the element.

7 Numerical Correlations with Experiments

The simplified uni-axial material and constitutive laws are implemented in the developed fiber beam element and analyzed the structural members under cyclic loading. Model predicted the experimental results throughout the loading history and could be used to simulate the behavior of RC structures under seismic loading.

7.1 Comparison of Concrete Model with the experimental 1-D Cyclic Stress–Strain Curves

The uni-axial material models developed in this paper are compared with the experimental results of Mansour (2001).

Mansour (2001) tested three panels of the CVE3—series. The steel grids in these panels are set parallel to the applied principal stresses in horizontal and vertical directions. The three panels of this series CVE3-1, CVE3-2 and CVE3-3 are subjected to 1-D cyclic loading in the horizontal direction, while maintaining a constant lateral tensile strain (ε_t) of 0.0044, 0.012 and 0.030.

Each panel has the following dimensions: length 1397 mm, height 1397 mm, and thickness 178 mm. The panels are reinforced in each direction with No. 6 bars at 267 mm spacing. The concrete compressive strengths of CVE3-1, CVE3-2, and CVE3-3 are 48, 41, and 43 MPa. The yield stress of longitudinal and transverse steel of panels CVE3-1, CVE3-2, and CVE3-3 are 425.4 MPa respectively.

The analytical result of the three panels CVE3-1, CVE3-2, and CVE3-3 with the current model and corresponding experimental results are presented in Figs. 8, 9, and 10. In these figures, the horizontal axes represent the smeared concrete strain in the longitudinal direction, and the vertical axes represent the smeared concrete stress in the longitudinal direction.

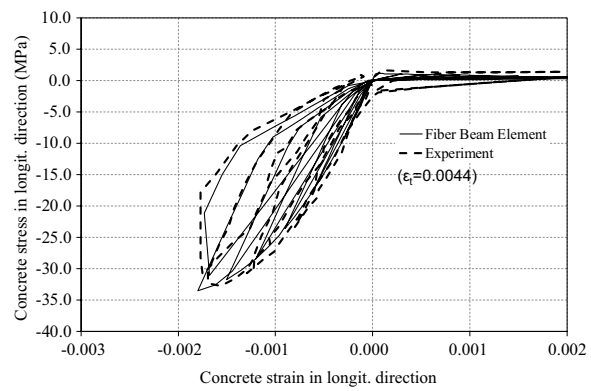

Fig. 8 Panel CVE3-1 concrete stress–strain behavior comparison with fiber beam element, and experiment (Mansour 2001).

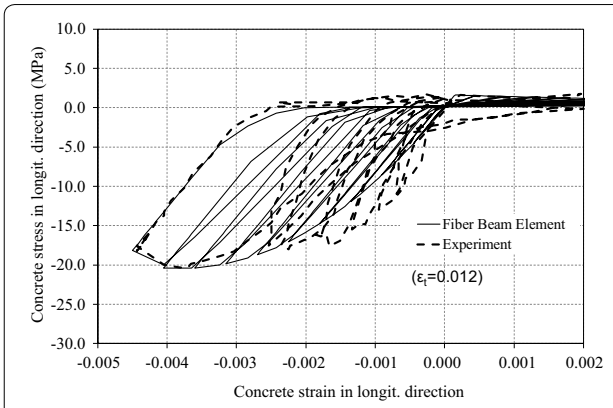

Fig. 9 Panel CVE3-2 concrete stress–strain behavior comparison with fiber beam element, and experiment (Mansour 2001).

Comparison of the current model results for the three panels in the CVE3 series showed an increase in lateral tensile strain; the ultimate value of the horizontal compression stress decreases because of the softening behavior of the concrete. Figures 8, 9, 10, 11, 12, 13 show that the current model predicts fairly well the experimental behavior at both the compression and tension regions.

7.2 Simulation of Columns

Three hollow, rectangular prototype bridge piers PI1, PI2, and PS1 are tested under reverse cyclical loading at the National Center for Research on Earthquake Engineering in Taiwan (Yeh and Mo 1999). These prototypes are analyzed using the fiber beam element. The specimens dimensions along with the material properties of concrete and reinforcement as given in Table 1. Figure 11 shows the details of the specimens' cross section dimensions and reinforcement details. The columns are tested

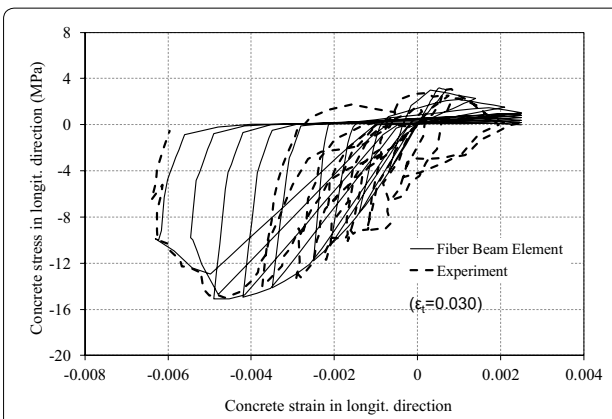

Fig. 10 Panel CVE3-3 concrete stress–strain behavior comparison with fiber beam element, and experiment (Mansour 2001).

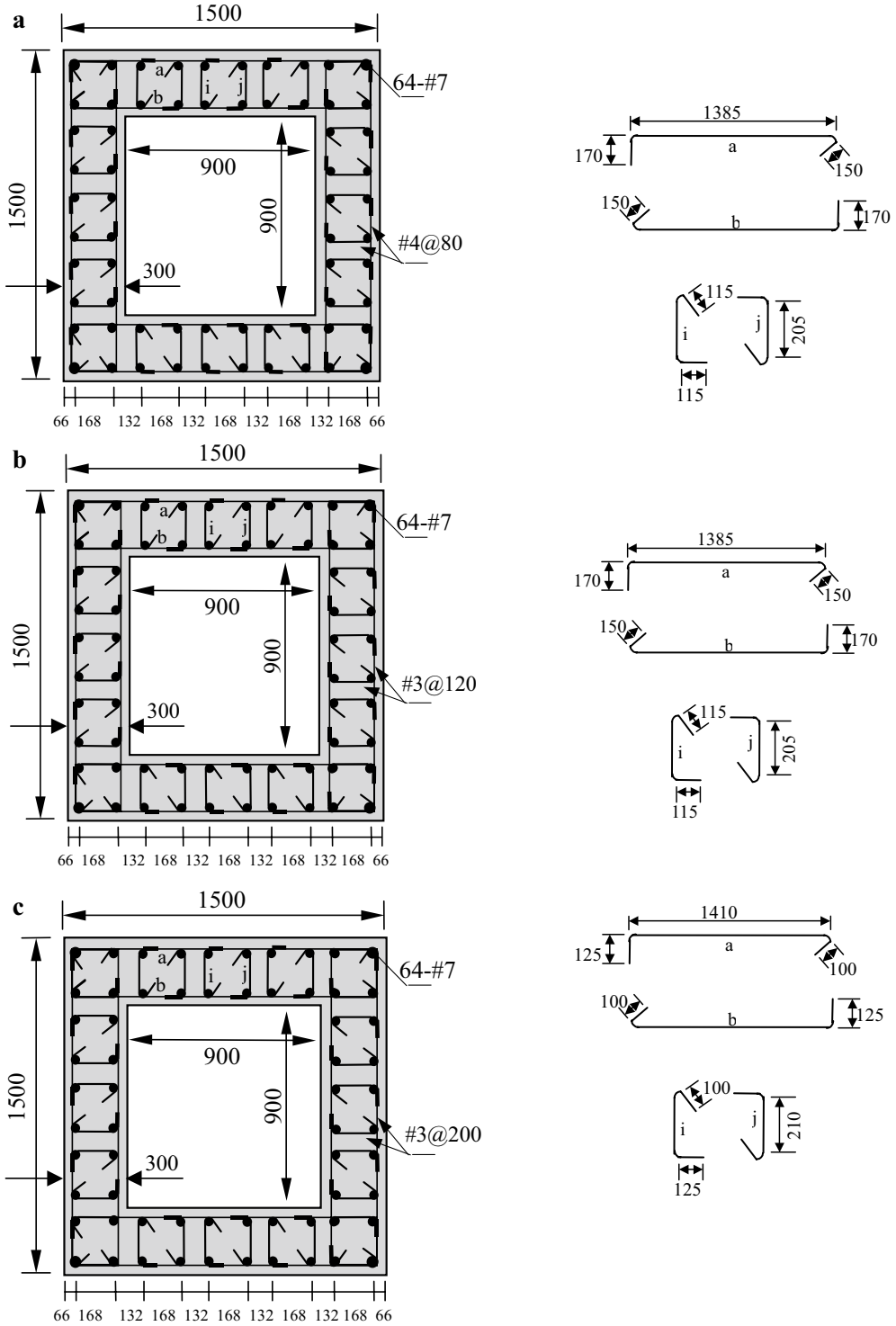

Fig. 11 Dimensions of cross sections and reinforcement details of specimens **a** PS1, **b** PI1 and **c** PI2 (Dimensions are in mm) (Yeh and Mo 1999).

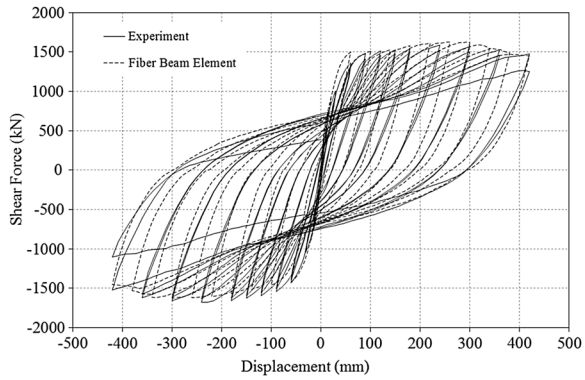

Fig. 12 Comparison of load–displacement behavior of specimen PS1 with fiber beam element, and experiment (Yeh and Mo 1999).

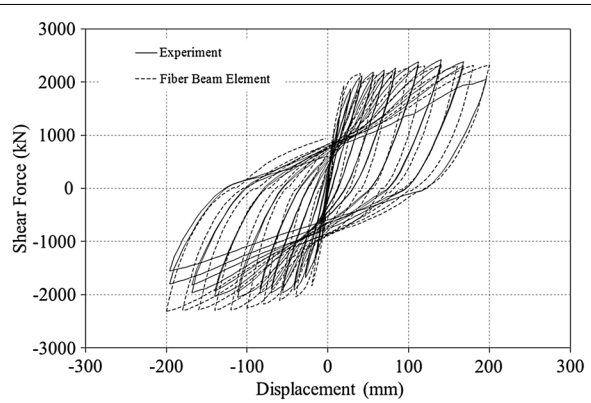

Fig. 13 Comparison of load–displacement behavior of specimen PI1 with fiber beam element, and experiment (Yeh and Mo 1999).

under displacement control with cyclically-reversed horizontal load.

The specimens are modeled with only one force based element and five Gauss–Lobatto integration points. The cross section is divided into 28 fiber sections. The boundary condition at the bottom is assumed to be fixed while the lateral load is applied to the top of the column. The longitudinal and transverse steel ratios are calculated based on the dimensions and spacing of the reinforcements. Concrete enveloped by the stirrups is modeled as confined concrete, while the remaining concrete (mostly in the cover) is considered as unconfined. The horizontal forces are increased based on the cyclic displacement control scheme.

The analytical shear force versus displacement relationships of the specimens are predicted with the 2-D fiber beam element as shown in Figs. 12, 13, 14; the results are then compared to the experimental data.

The moment arms for specimens PS1, PI1, and PI2 are 6.5, 4.5, and 3.5 m respectively. The reinforcement of the columns is designed such that column PS1 is dominated by a flexural failure, column PI1 is dominated by a flexure-shear failure, and column PI2 is dominated by shear failure. The experimental results (Yeh and Mo 1999) showed that specimens PS1 and PI1 failed in a flexure mode with the formation of plastic hinges at the bottom of the column and specimen PI2 failed under shear failure mode without rupturing the longitudinal reinforcement. The failure modes and ductility levels are reflected in the shape of the load displacement plots. The rebar yielded significantly prior to crushing of the concrete in specimens PS1 and PI1 (Figs. 12 and 13), which resulted in a long yield plateau and higher energy dissipation. Specimen PI2 (Fig. 14) showed a much shorter yield plateau and pinching with less energy dissipation

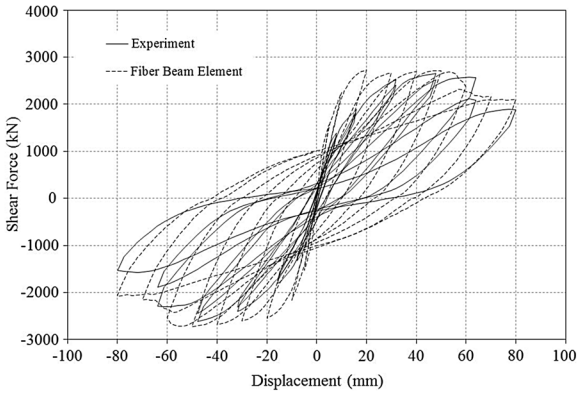

Fig. 14 Comparison of load–displacement behavior of specimen PI2 with fiber beam element, and experiment (Yeh and Mo 1999).

Table 1 Properties of bridge piers (Yeh and Mo 1999).

Specimen name	f_c' (MPa)	Length (mm)	Longitudinal reinforcement			Transverse reinforcement		
			Dia. (mm)	f_y (MPa)	f_{su} (MPa)	*Dia.* (mm)	f_y (MPa)	Spacing (mm)
PS1	34.0	6500	22	460.0	647.0	13	343.0	80
PI1		4500				10	510.0	120
PI2	32.0	3500		418.2	626.5	10	420.0	200

f_c', Concrete compressive strength; f_y, Steel yielding strength; f_{su}, Steel ultimate strength; *Dia.*, Diameter of steel bar.

Table 2 Comparison of strength values for specimens PS1, PI1, and PI2 (Yeh and Mo 1999).

Specimen	Strength in positive cycles (experimental)	Strength in positive cycles (analytical)	Strength in negative cycles (experimental)	Strength in negative cycles (analytical)
PS1	1580	1600	− 1620	− 1600
PI1	2300	2200	− 2050	− 2200
PI2	2700	2800	− 2700	− 2800

than specimens PS1 and PI1. Specimen PS1 developed a displacement ductility of 10.8, specimen PI1 developed a displacement ductility of 7.8, and specimen PI2 developed a displacement ductility of only 3.7.

The analytical load–displacement relationships with the fiber beam element accurately captured the different behaviors of each of the three specimens. The fiber beam element predicted the initial stiffness, yield point, ultimate strength, and ductility of specimens PS1 and PI1 very well. The predicted cyclic load–displacement curve of symmetric specimen PI1 (Fig. 13) showed less ultimate strength in the negative cycles compared to experimental results. The fiber beam element also predicted the behavior of specimen PI2 (Fig. 14) to a degree in the positive direction, including the ultimate strength and strength degradation in the descending branch. The predicted ultimate strength of specimen PI2 in the negative direction is slightly higher than the test result, while the ultimate strength is slightly less with the plane stress element analysis. The predicted hysteresis loops of specimen PI2 with fiber beam element showed much less energy dissipation and predicted the experimental results. Table 2 summarizes the specimens' strength values for both the experimental results and analytical predictions.

8 Conclusions

This paper represents a new element for cyclic analysis of reinforced concrete structures. A fiber-based beam element is developed to analyze reinforced concrete structures with the incorporation of mechanisms of shear deformation and strength. Simplified cyclic uni-axial constitutive relations are developed and checked with the 1-D cyclic test panels of Mansour (2001). The tangent stiffness is formulated with the inclusion of the softening and dilatation effects. The reverse cyclic analyses of different columns with rectangular cross-sections are analyzed with the 2-D fiber beam element. The cyclic analysis of columns tested by Yeh and Mo (1999) are analyzed with the 2-D fiber beam element. The columns with different aspect ratio exhibit different behaviors. The numerical results concerning the columns agree with the experimental data throughout the entire loading history. The finite element analysis using the generalized Softened Membrane Model predicted the experimental results throughout the loading history, including the initial stiffness, yield point, ultimate strength, and failure mode; and could therefore be used to simulate the behavior of RC structures under seismic loading.

Authors' contributions

TRM and AA developed the model presented. TRM conducted the computer coding and drafted the first version of the manuscript. Both authors read and approved the final manuscript.

Author details

[1] CTLGroup, 27834 Burchfield Grove Ln, Katy, TX 77494, USA. [2] Dept. of Civil Engineering, City University of London, Northampton Square, London EC1V OHB, UK.

Competing interests

The authors declare that they have no competing interests.

Publisher's Note

Received: 30 November 2017 Accepted: 26 June 2018
Published online: 01 October 2018

References

American Concrete Institute. (2008). *ACI 318, Building code requirements for structural concrete and commentary*. Farmington Hills, MI, USA: American Concrete Institute.

Belarbi, A., & Hsu, T. T. C. (1994). Constitutive laws of concrete in tension and reinforcing bars stiffened by concrete. *Structural Journal, American Concrete Institute, 91*, 465–474.

Belarbi, A., & Hsu, T. T. C. (1995). Constitutive laws of softened concrete in biaxial tension-compression. *Structural Journal of the American Concrete Institute, 92*(5), 562–573.

Filippou, F. C., Popov, E. P., Bertero, V. V. (1983). Effects of bond deterioration on hysteretic behavior of reinforced concrete joints. *Report SESM 77-1, Division of Structural Engineering and Structural Mechanics*. Berkeley: University of California.

Hsu, T. T. C., & Zhu, R. R. H. (2002). Softened membrane model for reinforced concrete elements in shear. *Structural Journal of the American Concrete Institute, 99*(4), 460–469.

Kupfer, H. B., Hildorf, H. K., & Rusch, H. (1969). Behavior of concrete under biaxial stresses. *Structural Journal, American Concrete Institute, 66*(8), 656–666.

Labib, M., Mullapudi, T. R. S., & Ayoub, A. S. (2013). Analysis of RC structures subjected to multi-directional shear loads. *Journal of Advanced Concrete Technology, 11*, 22–34.

Mansour, M. (2001). Behavior of reinforced concrete membrane elements under cyclic shear experiments to theory. *Ph.D. dissertation*. Department of Civil and Environmental Engineering, University of Houston.

Mullapudi, T. R. S., & Ayoub, A. S. (2009). *Fiber beam element formulation using the softened membrane model. American concrete institute special publication* (pp. 283–308). Farmington Hills: SP-265, ACI.

Mullapudi, T. R. S., & Ayoub, A. S. (2010). Modeling of the seismic behavior of shear-critical reinforced concrete columns. *Journal of Engineering Structures, 32*(11), 3601–3615.

Mullapudi, T. R. S., & Ayoub, A. S. (2013). Analysis of reinforced concrete columns subjected to combined axial, flexure, shear and torsional loads. *Journal of Structural Engineering ASCE, 139*(4), 561–573.

Pang, X. B., & Hsu, T. T. C. (1996). Fixed-Angle softened-truss model for reinforced concrete. *Structural Journal of the American Concrete Institute, 93*(2), 197–207.

Park, R., Priestley, M. J. N., & Gill, W. D. (1982). Ductility of square confined concrete columns. *Journal of Structural Davison, ASCE, 108*(4), 929–950.

Taylor, R. L. (2005). *FEAP User Manual v2.0.* Berkeley: Department of Civil and Environmental Engineering, University of California. http://www.ce.berkeley.edu/~rlt/feap/.

Vecchio, F. J. (1992). Finite element modeling of concrete expansion and confinement. *Journal of Structural Engineering, ASCE, 118*(9), 2390–2405.

Wang, J. (2006). Constitutive relationships of prestressed concrete membrane elements. *Ph.D. dissertation*. Houston: University of Houston.

Yeh, Y. K., Mo, Y. L. (1999). Full scale tests on ductility, shear strength and retrofit of reinforced concrete hollow columns (I). *Report, No. NCREE-99-024.* Taipei: National Center for Research on Earthquake Engineering. **(in Chinese)**.

Zhu, R. H., & Hsu, T. T. C. (2002). Poisson effect of reinforced concrete membrane elements. *Structural Journal, American Concrete Institute, 99*(5), 631–640.

Zhu, R. H., Hsu, T. T. C., & Lee, J. Y. (2001). Rational shear modulus for smeared crack analysis of reinforced concrete. *Structural Journal, American Concrete Institute, 98*(4), 443–450.